lubricants

MDPI

Article

Contact Load and Elastohydrodynamic Lubrication Analysis of Eccentric Bearings in RV Reducer Considering the Effects of Roller Profile Modification

Xinyue Zhang, Gang Wang *, Daqi Wu, Jian Guan * and Wenjie Chen

State Key Laboratory of High-End Heavy-Load Robots, Midea Group, Foshan 528311, China; zhangxy301@midea.com (X.Z.); wudq23@midea.com (D.W.); chenwj42@midea.com (W.C.)
* Correspondence: wanggang39@midea.com (G.W.); guanjian6@midea.com (J.G.)

Abstract: The mechanical and tribological behavior of eccentric bearings is crucial for the performance of a RV reducer. By combining the finite element model (FEM) and the elastohydrodynamic lubrication (EHL) method, a comprehensive model for the cylindrical roller bearings applied in the RV reducer is developed in this study. During the modeling phase, FEM is utilized to determine the bearing load, taking into account the structural flexibility. The FEM result demonstrates that a 15% increase in the maximum bearing's load is detected by the FEM compared to the analytical model. After the simulations, the effects of the roller profile modification, the bearing load and the rolling speed on the bearing performance are revealed. The numerical results indicate that the combined generatrix shape roller results in weaker edge effects and stress concentration compared with that of the straight generatrix shape roller and the arc generatrix shape roller. The optimal values of modification length and modification quantity under various load and rolling speed conditions are provided. Furthermore, durability tests on RV reducers equipped with the three types of rollers were conducted. Experimental outcomes demonstrate that the combined generatrix shape roller significantly improves the reliability and fatigue life of the RV reducer, corroborating the numerical analyses.

Keywords: RV reducer; eccentric bearing roller; tribo-mechanical performance; roller profile modification

Received: 14 November 2024
Revised: 10 December 2024
Accepted: 26 December 2024
Published: 3 January 2025

Citation: Zhang, X.; Wang, G.; Wu, D.; Guan, J.; Chen, W. Contact Load and Elastohydrodynamic Lubrication Analysis of Eccentric Bearings in RV Reducer Considering the Effects of Roller Profile Modification. *Lubricants* **2025**, *13*, 14. https://doi.org/10.3390/lubricants13010014

1. Introduction

The RV reducer is widely used in industrial robots considering the requirements for high accuracy, high reliability, high rigidity, heavy load and high power density [1]. In recent years, substantial efforts have been dedicated to the mechanical modeling of RV reducers. Research work of various domains, including the transmission error analysis [2,3], the stress concentration analysis [4,5], the reliability optimization [6,7], the efficiency optimization [8,9], and the tooth modification analysis were presented [10–12]. These investigations mainly focused on the transmission error and the behaviors of cycloid gear, and barely paid attention to the rolling bearing performance. In fact, rolling bearings are the principal load-carrying component in the RV reducer and significantly affect its precision and torsional rigidity [13]. Nowadays, the raceways of the bearing tend to integrate the shaft or housing, which makes the manufacturing and assembly process more complicated. Failure of the rollers is more likely to occur under heavy load conditions. To reveal the internal mechanics of rolling bearings and facilitate their optimal design, it is quite necessary to establish the theoretical model and conduct tribological experiments.

In order to obtain the load distribution of rolling bearings, several numerical models for RV reducers have been developed over the past decades. Addressing the impact of friction, Meng et al. [14] proposed a mathematical model to study the meshing transmission process of cycloid gears. This model accounts for backlash by integrating it with other geometrical parameters to ascertain the number of meshing teeth, subsequently employing mechanical equilibrium equations to calculate the gear load. A dynamic method that contains the differential equations of some components in the RV reducer was conducted by Zhang et al. [15]. In their analysis, the rolling bearing was equivalent to the stiffness spring to establish the dynamic equations. The load of the rolling bearing was obtained with the dynamic displacements and stiffness of the components. Yang [16] developed a dynamic approach containing crankshafts, cycloidal gears, needle bearings and planet carriers to investigate the internal load transmission characteristics within the RV reducer. The tooth profile of the cycloidal gear was discretized to judge the contact position between the gears and pins. The routine in their study was accomplished by the iterations of contact between the cycloidal gears and the pins. The bearing load can also be acquired by this method and the load distribution of the bearing is obtained through the calculation of radial migration. The model established by Hidaka et al. [17–19] is widely used in the area of industrial planetary reducer. In their model, each component of the RV reducer was considered as a 3-degree-of-freedom (DOF) rigid body and the equation considering 20 DOFs was finally established. In addition, the clearance of the bearings and the gear pins in the RV reducer was equivalent to the spring with experimentally determined stiffness. With their model, the displacements of all the components and the load of bearings considering different working conditions and design parameters can be analyzed.

In addition to the above studies, the optimization of the roller bearings has also received much attention. Guo et al. [20] presented an explicit matrix algorithm to calculate the elastic deformation of tapered rollers with three loaded surfaces. The results showed that the largest deformation appears at the larger end of the roller. An analysis of the impact of the contact angle revealed a marked increase in deformation concentration at the roller ends as the contact angle widened. Zhang et al. [21] studied the frictional torque of a dry-lubricated tapered roller bearing considering the effect of roller skewing. The results illustrated that a proper skewing angle is beneficial for torque reduction. In recent years, the elastohydrodynamic lubrication (EHL) methodology has been employed to assess the interaction and lubrication dynamics between rollers and raceways [22]. Marian et al. [23] studied the effect of surface texturing on friction and wear reduction, suggesting that micro-textures on the surfaces are helpful for enhancing energy efficiency and sustainability. Chen et al. [24], Zhao et al. [25], and Liu et al. [26] discussed the influence of roller profile on the pressure distribution and the film thickness. Based on the analysis, the best strategy for the roller profile was given. In the analysis presented by Zhu et al. [27], Qiu et al. [28] and Xiang et al. [29], the design parameters of the roller, such as contact length, crowning, chamfers and misalignment were considered. The results proved that EHL performance evaluation can be regarded as an engineering tool for roller design and optimization.

In contemporary engineering applications, straight generatrix shape rollers are prevalently utilized in RV reducers, leading to stress concentrations at the roller edges and the crankshaft surface. As the hardness of the bearing roller is higher than that of the crankshaft, the damage on the crankshaft is normally more severe, as observed in Figure 1. In contrast to the design alternation, the modification of the roller profile seems to be a more efficient strategy to reduce wear damage. The present paper aims to establish a numerical method to analyze the tribological behavior of rollers in RV reducer and evaluate the effect of the roller profile. The FEM is proposed to calculate the load distribution of eccentric bearings as the structural flexibility of the cycloidal gears has a significant effect on the bearing's

load distribution. Then, the EHL method is adopted to obtain the oil film pressure between the roller and the crankshaft surface considering the different modification profiles of the rollers. Finally, the tribological behavior of the contact pairs is discussed based on the numerical and experimental results.

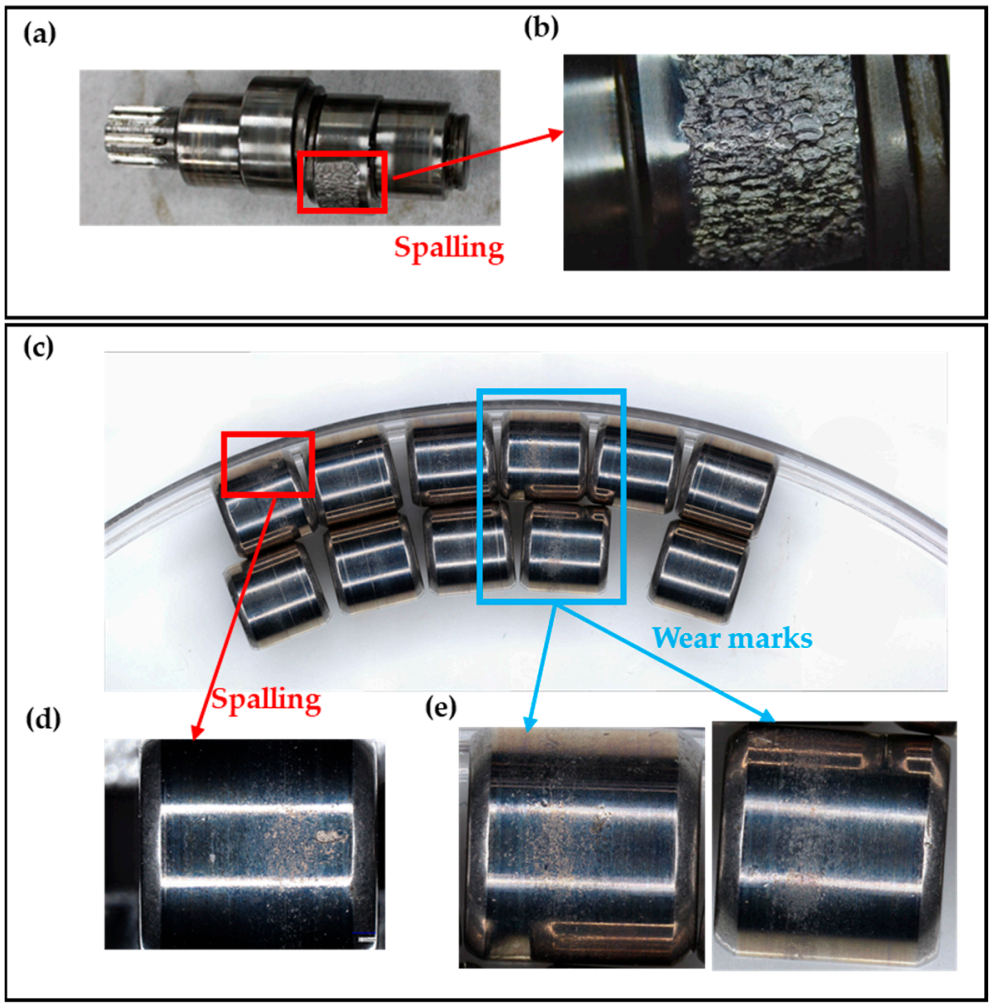

Figure 1. Damage on RV reducer. (**a**) spalling on crankshaft; (**b**) enlarged view of spalling on crankshaft; (**c**) wear and spalling on bearing rollers; (**d**) enlarged view of spalling on roller; (**e**) enlarged view of wear on rollers.

2. Theoretical Model

The RV reducer consists of six main components: planetary gears, crankshafts, cycloidal gears, pins, planetary carriers and bearings, as depicted in Figure 2. The transmission system involves low transmission ratio planetary gears and high transmission ratio cycloid gear pins. Therefore, the load is mostly carried by cycloidal gears and eccentric bearings with a 120° phase difference. In order to analyze the mechanical and lubrication performance of the eccentric bearings, a model combining FEM and EHL methods is proposed in this section. The simulation process is shown below: Firstly, the FEM of the RV reducer was established considering the six components. Secondly, the EHL method was adopted to calculate the oil film pressure between the rollers and the crankshaft. Then, the optimization of the roller's profile could be evaluated according to the response of oil film pressure.

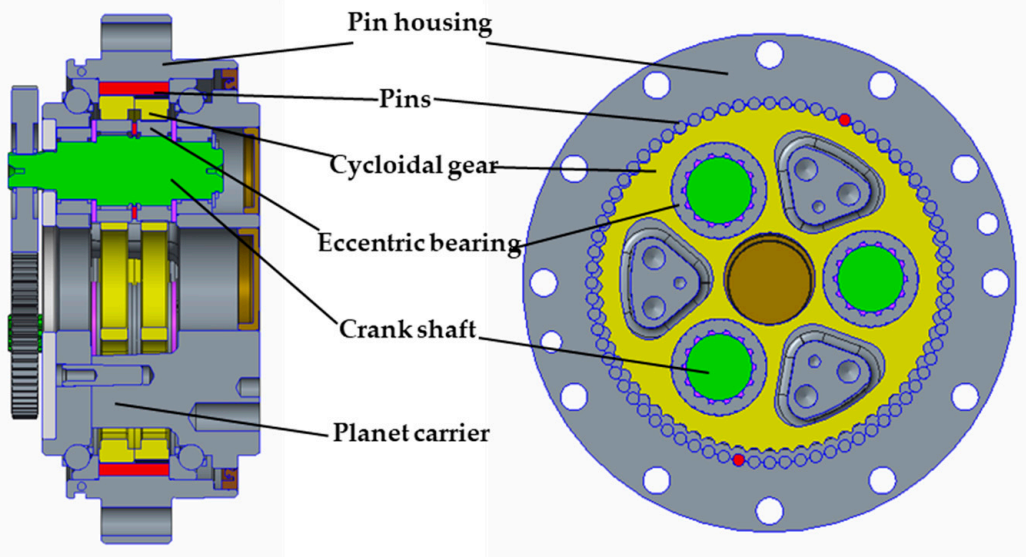

Figure 2. The components of RV reducer.

2.1. The FEM of RV Reducer

Figure 3 illustrates the FEM of the RV reducer. Three fan-shaped holes are designed on the spoke structure of the cycloidal gear to reduce weight as shown in Figure 3a (red square). The numerical models previously referenced [13,16–19] normally regard the cycloidal gear as a rigid body. However, the flexibility induced by the fan-shaped holes on the cycloidal gear would affect the load distribution of the bearings. FEM is preferable in mechanical analysis considering flexible structure. The meshing of the cycloidal gear and pins is shown in Figure 3b,c. The mesh size of the contact area and the structure away from the contact area were set to be 0.03 mm and 2 mm separately in order to obtain converged results and acceptable calculation time. The coefficient of friction between the cycloidal gear and pins is 0.05. The whole FEM of the RV reducer (Figure 3e) in this manuscript was integrated with solid elements, contact elements and spring elements to balance simulation time cost and accuracy [30,31]. Solid 187 element was applied on the cycloidal gears, crankshaft and planet carrier as shown in Figure 3c,d,f. The rollers of the eccentric bearings (Figure 3g) were simulated with the combine 39 element as depicted in Figure 3h. Contact 174 element and target 170 element were utilized on the contact surface of the cycloidal gear pins to transfer the contact load (Figure 3c). All DOFs of the nodes on the outermost face of the pin housing are constrained. The load is applied to the center of the planet carrier and the center node is connected to the planet carrier by rigid elements. The working conditions of the RV reducer are listed in Table 1.

Table 1. The working conditions of RV reducer.

Nominal Load (Nm)	Ultimate Load (Nm)	Nominal Speed (rpm)	Ultimate Speed (rpm)	Lubricants
500	1250	1400	5600	Castro ALR

Figure 4 gives the mesh sensitivity results of the FEM. There is no doubt that both the maximum contact pressure of gear pins and the maximum force of eccentric bearings reach a stable level when the mesh size is lower than 0.03 mm.

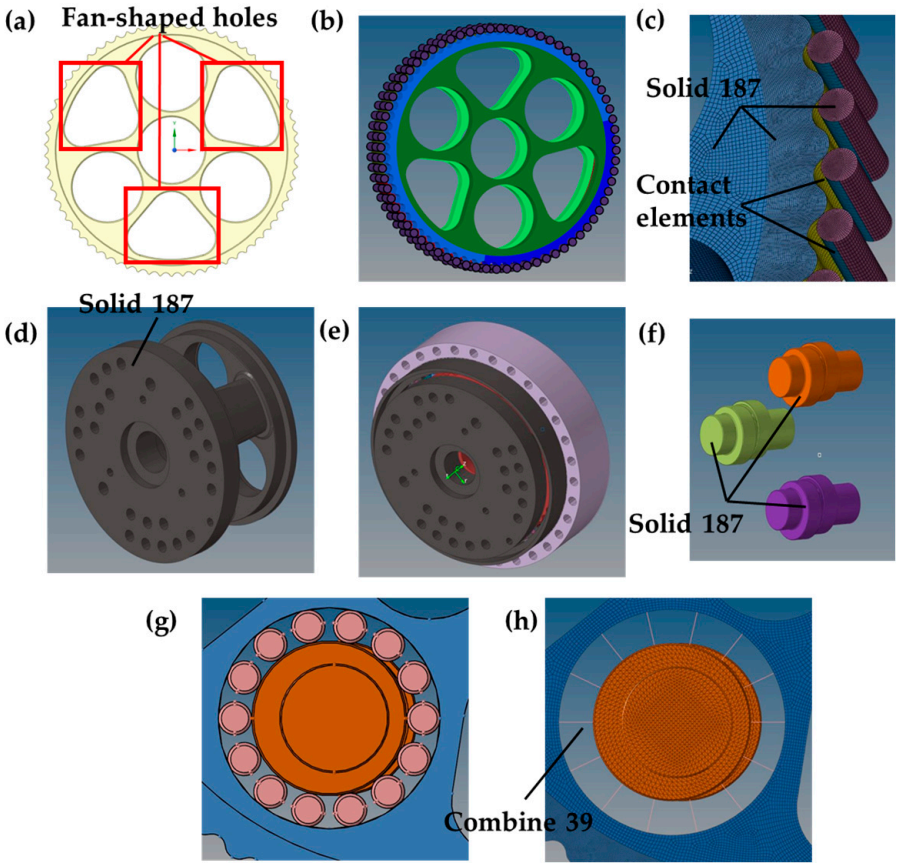

Figure 3. The FEM of RV reducer. (**a**) structure with fan-shaped holes; (**b**) mesh of cycloidal gear and pins; (**c**) fine mesh of the contact area; (**d**) mesh of planet carrier; (**e**) mesh of the RV reducer; (**f**) mesh of crankshaft; (**g**) structure of eccentric bearing; (**h**) mesh of eccentric bearing.

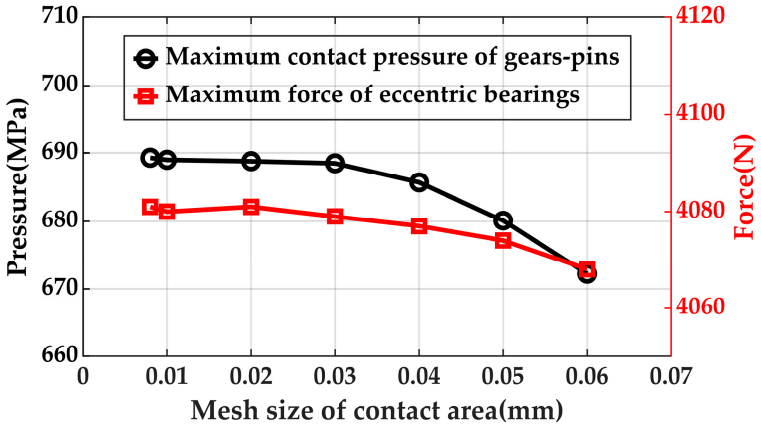

Figure 4. The mesh sensitivity results of FEM.

2.2. Lubrication Analysis of Bearing Roller Crankshaft

The EHL model is established in this section to analyze the oil film pressure between the bearing roller and the crankshaft. The Reynolds equation of the solution domain [32] can be expressed as:

$$\frac{\partial}{\partial X}\left(\frac{\rho h^3}{12\eta}\frac{\partial P}{\partial X}\right)+\frac{\partial}{\partial Z}\left(\frac{\rho h^3}{12\eta}\frac{\partial P}{\partial Z}\right)=U\frac{\partial(\rho h)}{\partial Z}+\frac{\partial(\rho h)}{\partial t} \quad (1)$$

where ρ is the density of the lubricant, η is the effective viscosity of the lubricant, P is the oil film pressure of the solution domain, h is the film thickness of the solution domain, U is

the relative entraining speed of the bearing roller and crankshaft, Z represents the rolling direction of the roller and X is the roller axis direction.

Film thickness h at a specific location can be expressed in Equation (2):

$$h(X, Z, t) = h_0(t) + f(X, Z, t) + V_e(X, Z, t) \tag{2}$$

where $h_0(t)$ is the normal gap of the two bodies, $f(X, Z, t)$ is the clearance considering bodies' geometry before elastic deformation, $V_e(X, Z, t)$ is the elastic deformation.

The elastic deformation of the two bodies is expressed as Equation (3). The whole solution domain is divided into substantial discrete domains. The total elastic deformation of a single point (X, Z) can be integrated by the force of all the discrete domains.

$$V_e(X, Z, t) = \frac{2}{\pi E'} \iint_{\Omega} \frac{P(\varepsilon, \vartheta, t)}{\sqrt{(X-\varepsilon)^2 + (Z-\vartheta)^2}} d\varepsilon d\vartheta \tag{3}$$

where E' is the equivalent elastic modulus, Ω is the solution domain, ε and ϑ represent the integrating coordinates of solution domain Ω.

The Roelands law [32] is the most widely used pressure–viscosity model and the expression of the model is given as follows:

$$\eta = \eta_0 \exp\left\{ (\ln\eta_0 + 9.67) \left[\left(1 + 5.1 \times 10^{-9} P\right)^{Z'} - 1 \right] \right\} \tag{4}$$

where η_0 is the lubricant viscosity at the ambient pressure, Z' is the pressure–viscosity index, Z' can be calculated by $Z' = \frac{a'}{5.1 \times 10^{-9}(\ln\eta_0 + 9.67)}$, a' is the pressure–viscosity exponent.

The pressure–density equation is expressed as follows:

$$\rho = \rho_0 \left(1 + \frac{0.6 \times 10^{-9} P}{1 + 1.7 \times 10^{-9} P} \right) \tag{5}$$

where ρ_0 is the lubricant density at the ambient pressure.

In the solution domain, the load applied on the bearing roller crankshaft is balanced by the integral of the pressure distributed in the domain:

$$w(t) = \iint_{\Omega} P(X, Z, t) dX dZ \tag{6}$$

It should be noted that the Reynolds number of the lubricating oil between the roller and the crankshaft is lower than 2.1 under the operating condition of the RV reducer in our research work. The lubricating oil is in the status of streamline flow as the Reynolds number is lower than 2×10^5 [33]. The Reynolds number can be calculated by the following equation and the values of the variables in Equation (7) are listed in Table 2.

$$R_e = \frac{\rho U L}{\eta} \tag{7}$$

where L is the specific length of the contact region.

Table 2. The values of parameters in Equation (7) and lubricating oil (Castro ALR) properties.

ρ (Kg/m^3)	U (m/s)	L (m)	η (Pa·s)	a'
870	0.05–0.562	23–175 $\times 10^{-6}$	40.3 $\times 10^{-3}$	1.28 $\times 10^{-8}$

The whole solving steps of the numerical methods are given as follows: First, the FEM is solved and the resultant force of the eccentric bearing is obtained. Further, the sliding

velocity and the maximum Hertzian contact pressure between the roller and the crankshaft are calculated by the numerical method in Reference [34]. Finally, the EHL performance of the contact region between the roller and the crankshaft, including oil film pressure, contact region width and film thickness is acquired by taking the sliding velocity and the maximum Hertzian contact pressure as initial working conditions. In this paper, the X and Z axes represent the roller's axis direction and rolling direction, respectively. Hence, the solution domain is in the X-Z plane. The oil film pressure distribution within the solution domain can be obtained by solving the governing Equation (1) using the multi-grid method. In order to solve the EHL equations, the oil film is divided into five layers, and the top layer has 1024 nodes in the X direction and 128 nodes in the Z direction. The convergence of the EHL equations is achieved when the error of the absolute pressure is lower than 1×10^{-3}. A detailed introduction to the multi-grid method can be found in Reference [35]. It can be easily realized that the oil film pressure is sensitive to the film thickness $h(X, Z, t)$, which contains contact bodies' geometry clearance and elastic deformation. Notably, the elastic deformation of the contact bodies as described in Equation (3) is induced as the interaction between lubricating oil and contact bodies in EHL theory. The lubricant viscosity and density are functions of oil film pressure P and are variable in the solution domain.

2.3. Modification of Roller's Profile

Rollers applied in the eccentric bearings of the RV reducer are usually designed with straight generatrix and round corners as shown in Figure 5. The equation of the roller's profile is expressed as Equation (8). Typically, stress concentration is induced at the location of the round corners. Hence, modification of the profile of the roller is certainly necessary. In this section, two types of profiles are generated to investigate the effect of the roller's shape on the pressure distribution as illustrated in Figure 6.

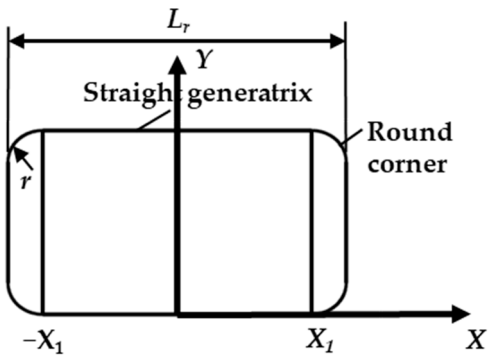

Figure 5. Profile of straight generatrix shape roller.

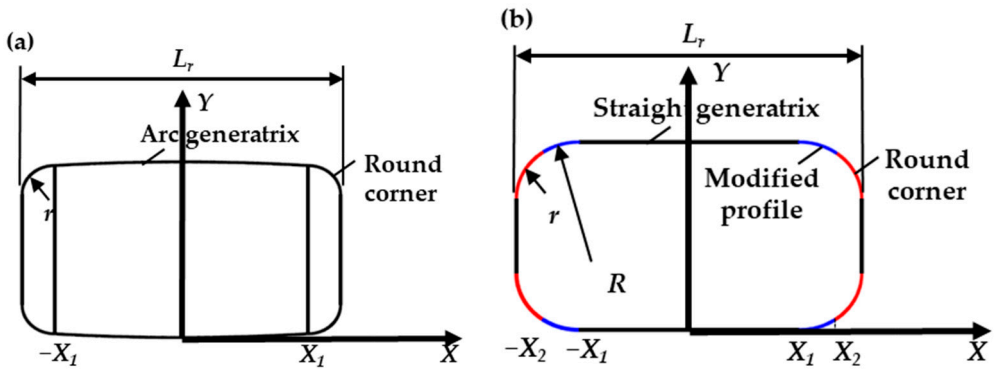

Figure 6. Roller with other types of profile. (**a**) arc generatrix shape roller; (**b**) combined generatrix shape roller.

The equation of straight generatrix shape roller:

$$Y = 0 - X_1 \le X \le X_1 \tag{8}$$

(1) The arc generatrix shape roller

The generatrix of the roller is generated in arc shape with round corners as shown in Figure 6a. The curve can be expressed in Equation (9):

$$Y = R - \sqrt{R^2 - X^2} - X_1 \le X \le X_1 \tag{9}$$

where r refers to the radius of the round corner, and R is the radius of the arc curve.

It should be noted that the clearance $f(X, Z, t)$ in Equation (2) can significantly affect the oil film pressure between the two bodies. The value of $f(X, Z, t)$ is obtained by Equation (9).

(2) The combined generatrix shape roller

Figure 6b shows the profile of the combined generatrix shape roller which consists of three segments: straight segment, modified segment and round corner. The equation of the roller's profile can be expressed as follows:

$$\begin{cases} Y = 0 - X_1 \le X \le X_1 \\ Y = R - \sqrt{R^2 - (-X_1 - X)^2} - X_1 - a \le X < -X_1 \\ Y = R - \sqrt{R^2 - (X - X_1)^2}\ X_1 < X < X_1 + a \end{cases} \tag{10}$$

where r refers to the radius of the round corner, R is the radius of the modified segment curve, a denotes the length of the modified segment, $a = X_2 - X_1$, b is the quantity of the modified segment, $b = R - \sqrt{R^2 - a^2}$. The value of $f(X, Z, t)$ is determined by a, b and R.

3. Numerical Results

3.1. Load Distribution of the Eccentric Bearings

To explore the impact of the flexibility of the cycloidal gears on the load distribution of bearings, this study incorporates an analytical approach as detailed in Reference [36]. Figure 7 illustrates the eccentric bearings' load distribution induced by the contact force between cycloidal gear and pins. The load on each eccentric bearing contains two parts: force induced by cycloidal gear pins and force induced by torque T. The load of the eccentric bearings can be expressed as Equations (11) and (12).

$$\begin{cases} \boldsymbol{F_A} = \boldsymbol{F_{A1}} + \boldsymbol{F_{A2}} = \frac{\boldsymbol{F}}{3} + \frac{F_t r'_c}{3a_0} \begin{Bmatrix} \sin(0^\circ) \\ -\cos(0^\circ) \end{Bmatrix} \\ \boldsymbol{F_B} = \boldsymbol{F_{B1}} + \boldsymbol{F_{B2}} = \frac{\boldsymbol{F}}{3} + \frac{F_t r'_c}{3a_0} \begin{Bmatrix} \sin(120^\circ) \\ -\cos(120^\circ) \end{Bmatrix} \\ \boldsymbol{F_C} = \boldsymbol{F_{C1}} + \boldsymbol{F_{C2}} = \frac{\boldsymbol{F}}{3} + \frac{F_t r'_c}{3a_0} \begin{Bmatrix} \sin(240^\circ) \\ -\cos(240^\circ) \end{Bmatrix} \end{cases} \tag{11}$$

$$\boldsymbol{F} = F \begin{Bmatrix} \sin(\alpha_c - \theta) \\ \cos(\alpha_c - \theta) \end{Bmatrix} \tag{12}$$

where $\boldsymbol{F_A}$, $\boldsymbol{F_B}$ and $\boldsymbol{F_C}$ denote the force vector of three eccentric bearings of a single cycloidal gear, $\boldsymbol{F}$ is the force vector of cycloidal gear and pins, r'_c refers to the pitch circle radius of cycloidal gear pins, a_0 is the distributed radius of the crankshaft, F_t is the tangential force of cycloidal gear and pins, $F_t = T/(r'_c)$, T is the torque load on the single cycloid gear,

α_c is the angle between $\boldsymbol{F}$ and $\boldsymbol{F_t}$, θ is the rotational angle of the crankshaft. The detailed calculating process of $\boldsymbol{F}$ in the analytical method can be found in [36].

The following assumptions are adopted in the analytical method:

1. The whole cycloidal gear is regarded as a rigid body and the contact force $\boldsymbol{F}$ is evenly assigned among the three eccentric bearings;
2. The torque T is also evenly distributed by the three eccentric bearings;
3. The magnitude of the forces in (1) and (2) for three eccentric bearings is exactly the same yet the resultant force of the bearing is determined by the magnitude and crankshaft rotational angle θ.

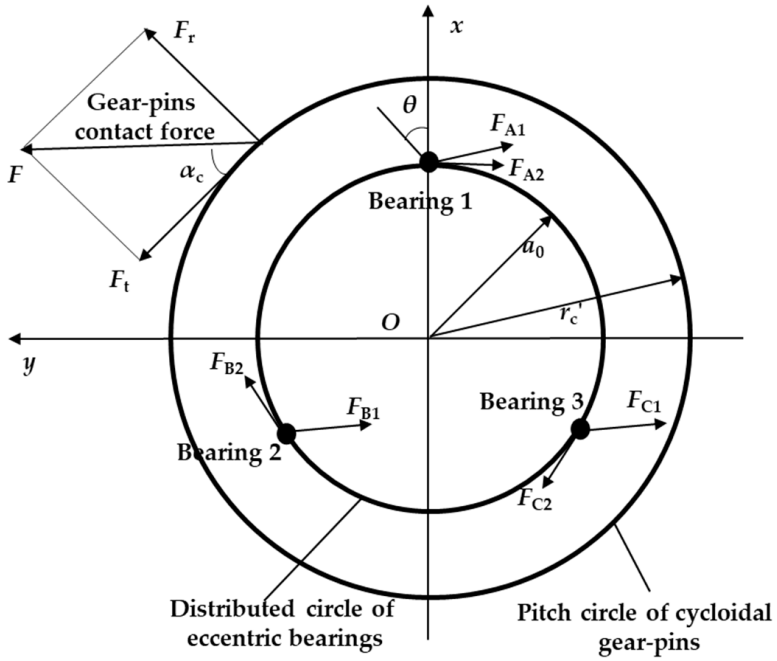

Figure 7. The load distribution induced by the contact force of cycloidal gear pins.

Figure 8 depicts the resultant force of the eccentric bearings in the RV reducer. In Figure 8a, the variation of a single eccentric bearing's force considering the rotational of the crankshaft by three numerical models is presented. The analytical result of the bearing's resultant force is obtained by solving analytical Equation (11). A different FEM from which the fan-shaped holes in the cycloidal gears are omitted is presented for comparison in Figure 9. As the fan-shaped holes of the cycloidal gears are removed, the rigidity of the reducer is higher. It can be observed that the force distribution curve presents like a cosine curve with the rotating of the crankshaft. Note that the maximum force and minimum force obtained from the FEM (cycloidal gears without holes) are nearly the same as that of the analytical model. Compared to the analytical model, the maximum value and the minimum value of the FEM (cycloidal gears with holes) increase by about 15% and 26%, respectively. This is due to the uneven local deformation of the cycloidal gear while considering the flexibility of the cycloidal gear (red square area in Figure 3a). Special attention should be focused on structural flexibility in the case of RV reducer's force analysis.

Figure 8b shows the load distribution of three eccentric bearings in a single cycloidal gear as the rotating of the crankshaft by FEM. During the rolling process, the maximum and minimum load value of the bearing is almost the same. The phase difference of the three bearings' load is approximately 120°. The calculation results illustrated in Figure 8 match the mechanical rules of the RV reducer [16,36]. It can be confirmed that FEM is preferable compared to other methods while considering structural flexibility. The forces deduced

from the FEM subsequently serve as the foundational load conditions for subsequent lubrication analysis.

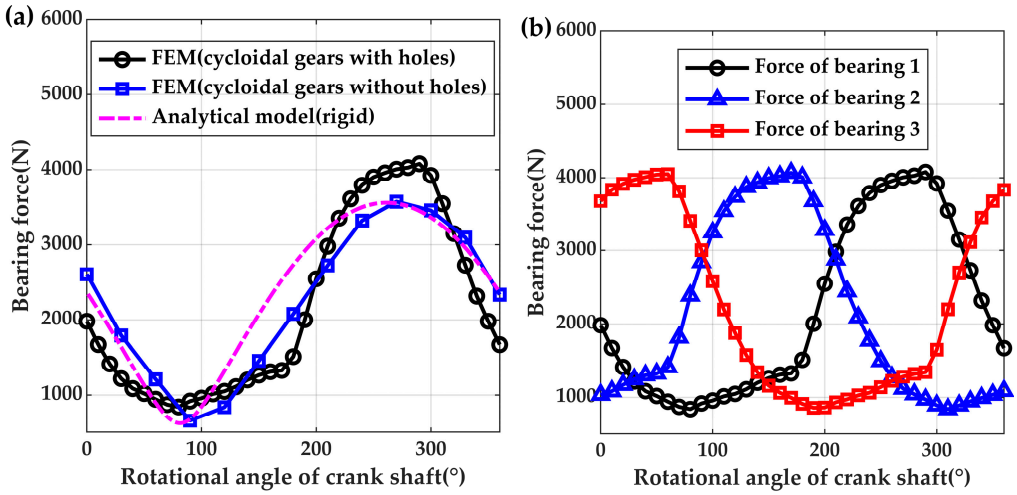

Figure 8. Resultant force of eccentric bearings. (**a**) comparison of eccentric bearing's force among different numerical methods; (**b**) three eccentric bearings' force during one rotational cycle of the crankshaft.

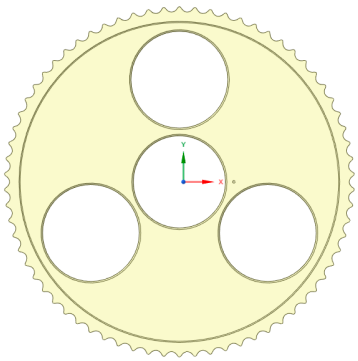

Figure 9. Cycloidal gear without fan-shaped holes.

In order to analyze the effect of the roller's profile modification on EHL, numerical analyses are conducted in Sections 3.3 and 3.4. In these cases, the load applied on the single roller is 1978 N which is obtained by the FEM in Section 3.1. The sliding velocity between the roller and crankshaft is 0.101 m/s (corresponds to the nominal speed of the RV reducer) which is calculated by the method proposed in Reference [34].

3.2. Verification of EHL Method

Figure 10 depicts the contact of the bearing roller and crankshaft, which is predicted as a cylindrical contact. X and Z axes represent the roller's axis direction and rolling direction, respectively. The idealized Hertzian line contact pressure distribution equation is listed as Equation (13). Variable ph is introduced as the maximum contact pressure calculated by Equation (14).

$$\sigma = \mathrm{ph}\left[1 - (Z/b_w)^2\right]^{0.5} \tag{13}$$

$$\mathrm{ph} = 2Q/(\pi L_r b_w) \tag{14}$$

where b_w equals to 95 μm, the value of L_r is 8.5 mm, Q refers to the contact load and is equivalent to 1978 N as calculated in Section 3.1.

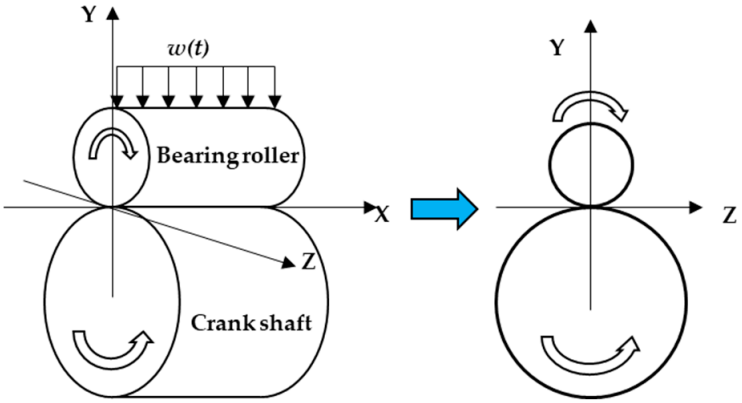

Figure 10. The cylindrical contact of the bearing roller and crankshaft.

Figure 11 illustrates the pressure distribution of the straight generatrix roller obtained by the EHL method (Equation (1)) and Hertzian method (Equation (13)). The two-dimensional oil film pressure calculated by the EHL method is shown in Figure 11a. It can be obviously seen that pressure concentration occurs at the edges of the roller. In Figure 11b, the *Y*-*Z* plane contact pressure remains identical along the axis direction of the roller in idealized Hertzian theory. The pressure of the *Y*-*Z* plane ($X = 0$) of Figure 11a,b is illustrated in Figure 11c. The result in Figure 11c indicates that the oil film pressure obtained by the EHL method is reliable and accurate. Viewing from the EHL oil film pressure distribution curve, an obvious pressure spike in the outlet of the contact region is generated. The value of ph is equivalent to 1.56 GPa as shown in Figure 11c. The results of Figure 11 are in accordance with that in Reference [27].

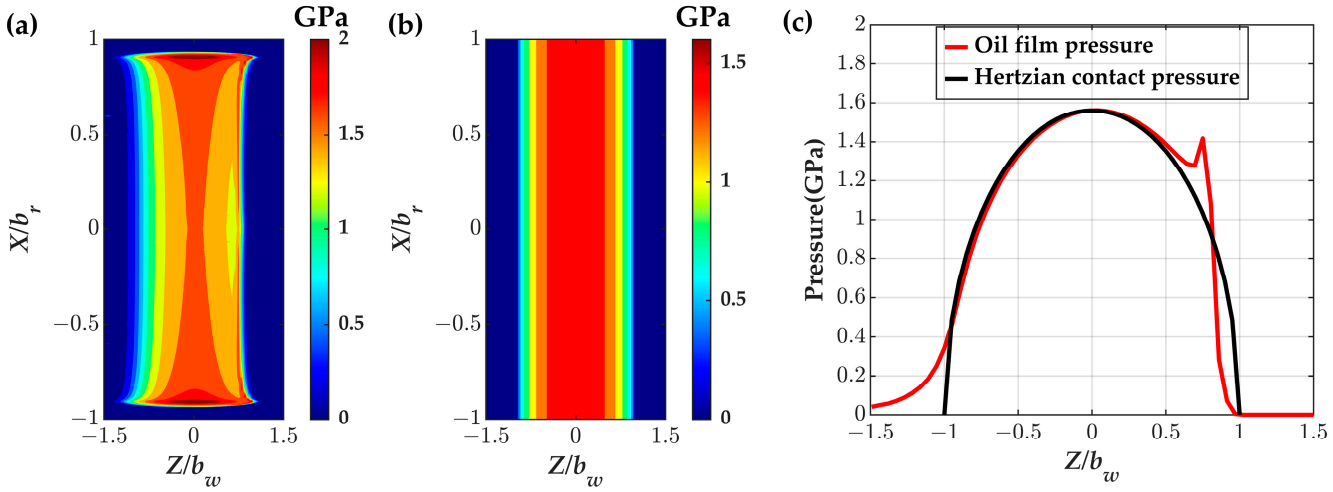

Figure 11. Pressure distribution obtained by the EHL method and Hertzian method. (**a**) two-dimensional oil film pressure distribution; (**b**) two-dimensional contact pressure distribution; (**c**) comparison of pressure by the two methods in *Y*-*Z* plane ($X = 0$).

3.3. Effects of Arc Generatrix on EHL Performance

In this section, the effect of the profile's arc radius on EHL performance is investigated by considering oil lubrication. As described in Section 2.2, the oil film pressure distribution P of the solution domain in the *X*-*Z* plane between the roller and the crankshaft can be obtained by solving Equation (1). The oil film pressure distribution considering varying arc radius with constant L_r and r values ($b_r = L_r/2$) along the roller axis direction (*X* axis, $Z = 0$) is illustrated in Figure 12a. The oil film pressure distribution along the roller axis direction (*X* axis, $Z = 0$) can be significantly affected by arc radius as $f(X, Z, t)$ changes obviously with varying arc radius. In addition, the result of a straight generatrix shape roller (the

black curve in Figure 12a) is induced to compare. The analysis reveals a pronounced edge effect in the case of the straight generatrix shape roller, increasing the propensity for damage at the roller's edges. Therefore, damage is more likely to generate at the edge of the roller. Profile modification is necessary for the roller in order to decline the edge effect. Arc generatrix is the most familiar modified profile for rollers from a theoretical view. The contact state converts to point contact in the case of arc generatrix and damage is most likely to appear at the middle segment of the roller. As the arc radius decreases from 1020 mm to 100 mm, the maximum oil film pressure increases from 1.32ph to 1.95ph. In contrast, the maximum oil film pressure induced by the edge of the straight generatrix shape roller is 1.24ph. In order to further decrease the stress concentration, the radius of the roller needs to be raised to a higher value. The modification quantity at the edge of the roller is difficult to ensure with a higher radius value due to limitations in the mechanical machining capacity. Hence, this paper will not investigate the roller's profile whose modification quantity is less than 5 μm (the arc radius of 1020 mm corresponds to a modification quantity value of 5 μm).

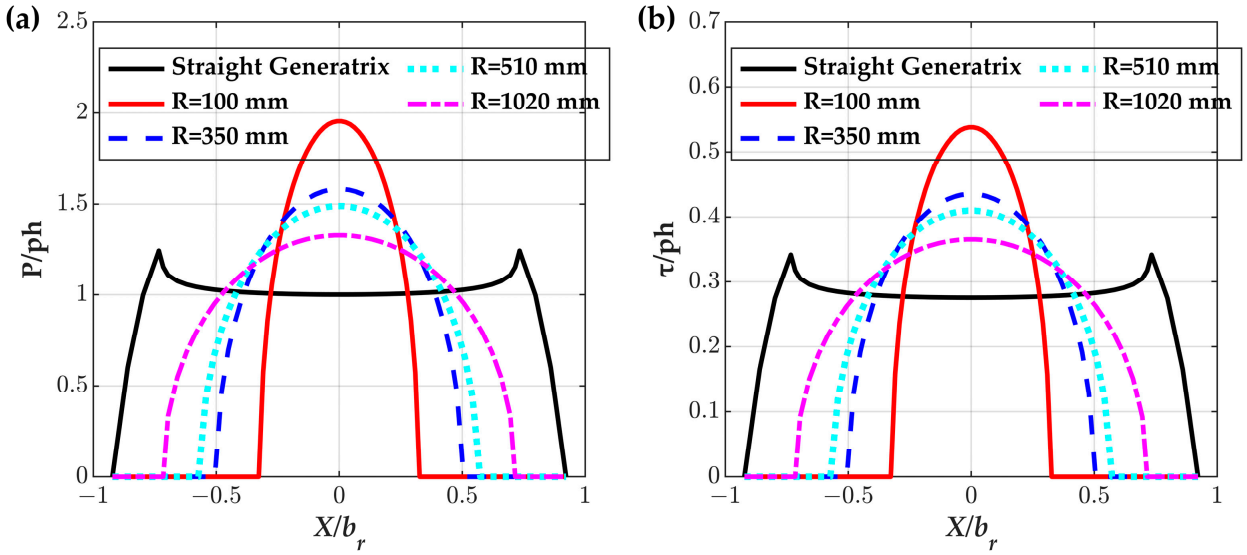

Figure 12. Pressure and shear stress distribution along the roller's axis considering varying arc radius. (**a**) pressure distribution; (**b**) maximum shear stress distribution.

The shear stress in the *Y*-*Z* plane is calculated by Equation (15) [37]. The shear stress is integrated by the pressure distribution of the *Y*-*Z* plane. Then, the maximum shear stress τ along the roller axis direction (*X* axis) is depicted in Figure 12b. The fatigue damage may initiate from the stress concentration sites. The results above suggest that the roller with a single generatrix does not behave well during the rolling process. This clearly indicates the necessity for implementing a comprehensive modification strategy to obtain better lubrication performance.

$$\tau_{yz} = -\frac{2Y^2}{\pi}\int_{-b_w}^{b_w}\frac{P(s)(Z-s)ds}{\left\{(Z-s)^2+Y^2\right\}^2} - \frac{2Y}{\pi}\int_{-b_w}^{b_w}\frac{q(s)(Z-s)^2ds}{\left\{(Z-s)^2+Y^2\right\}^2} \quad (15)$$

where *Z*, *Y* refers to the rolling direction and depth direction, b_w is the contact half-width, $P(s)$ is the pressure distribution, $q(s)$ is the contact friction distribution, $q(s) = \mu \times P(s)$, μ is set to be 0.05 in this paper.

3.4. Effects of Combined Generatrix Profile Modification on EHL Performance

This section examines the impact of modification quantity b and modification length a to identify the best values that decrease the oil film pressure and the maximum shear stress. The oil film pressure and maximum shear stress distribution along the roller axis direction (X axis) would be influenced by the modification parameters as a, b and R determine $f(X, Z, t)$ in Equation (2). Figure 13 illustrates the oil film pressure and maximum shear stress distribution along the roller's axis direction, with a focus on the effects of b. The straight generatrix shape roller can be regarded as the situation of b = 0 μm. As the modification quantity increases from 5 μm to 15 μm, the maximum oil film pressure and the maximum shear stress grow simultaneously. It can be explained as the radius R in Figure 6b decreases with the rising of modification quantity b, which aggravates the geometric discontinuity of the straight segment and modified segment. A further novel finding is that a modification quantity of 0 μm (straight generatrix) could also induce oil film pressure and maximum shear stress increasing at the roller's edges. This phenomenon demonstrates that a turning point exists as the modification quantity increases from 0 μm to 15 μm.

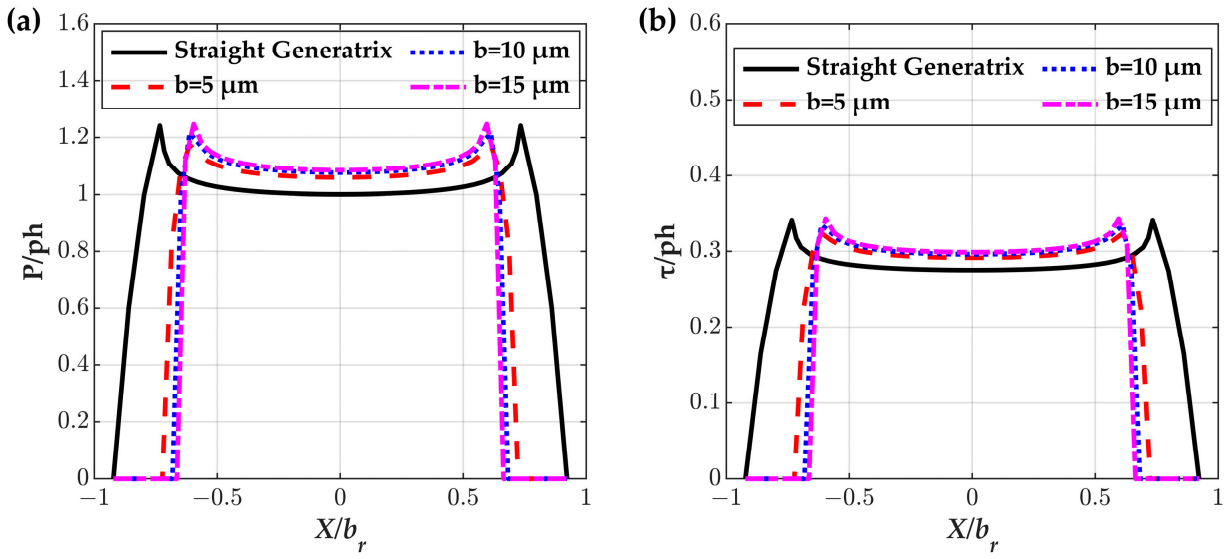

Figure 13. Pressure and shear stress distribution along the roller's axis considering modification quantity. (**a**) pressure distribution; (**b**) maximum shear stress distribution.

Figure 14 depicts the effects of modification quantity and modification length on maximum oil film pressure and maximum shear stress. It can be seen from Figure 14a that the oil film pressure and the maximum shear stress rise sharply with the decreasing of modification quantity in the range of 0 μm to 0.6 μm due to the severe edge effect induced by smaller-scale clearance (less than 1 μm) of bearing rollers. The modification quantity of 0.5–0.8 μm seems to be a good choice for the roller's profile from a theoretical view. However, the modification quantity is nearly impossible to reach to the value of less than 5 μm constrained to the mechanical machining capacity. Therefore, the modification quantity value of 5–10 μm is preferable.

Figure 14b illustrates the effect of modification length on maximum oil film pressure and maximum shear stress. The modification length value for the best EHL performance is about 1.2 mm. The oil film pressure and the maximum shear stress reach a relatively lower level which can enhance the fatigue life of roller bearing.

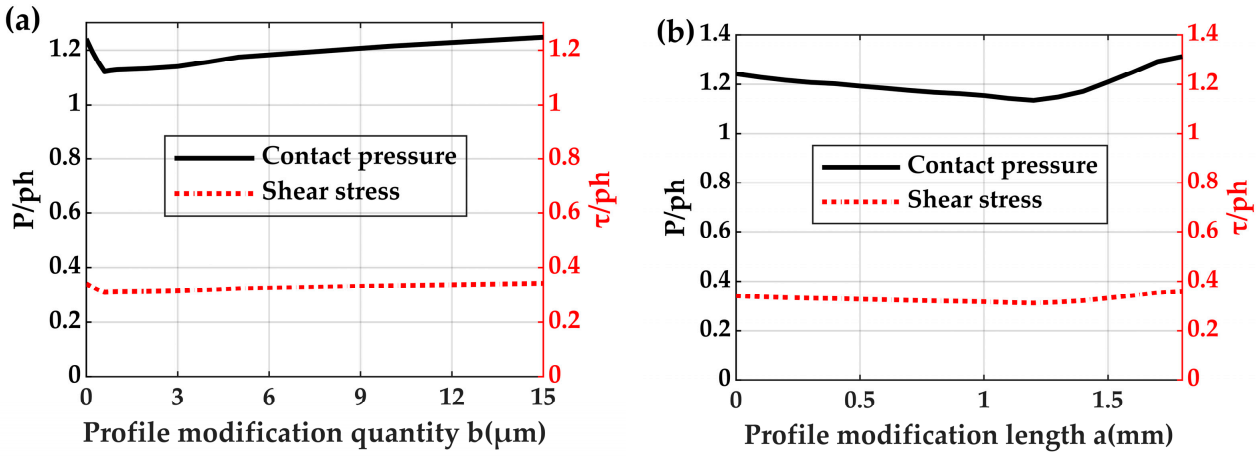

Figure 14. Effects of modification parameters on maximum pressure/shear stress. (**a**) modification quantity's effect; (**b**) modification length's effect.

3.5. Effects of Operating Load and Speed on EHL Performance

Figure 15 illustrates the oil film pressure and the maximum shear stress distribution along the roller's axis direction considering varying operating loads. In Figure 15, nominal load and ultimate load are given in Table 1 and medium load equals 875 Nm. The operating speed of the RV reducer is 1400 rpm with a sliding velocity of 0.101 m/s. With the increasing operating load, both the oil film pressure and the maximum shear stress rise obviously. Additionally, a larger contact region is observed in case of a higher load. The stress concentration can be weakened by applying the modification method in Section 2.2.

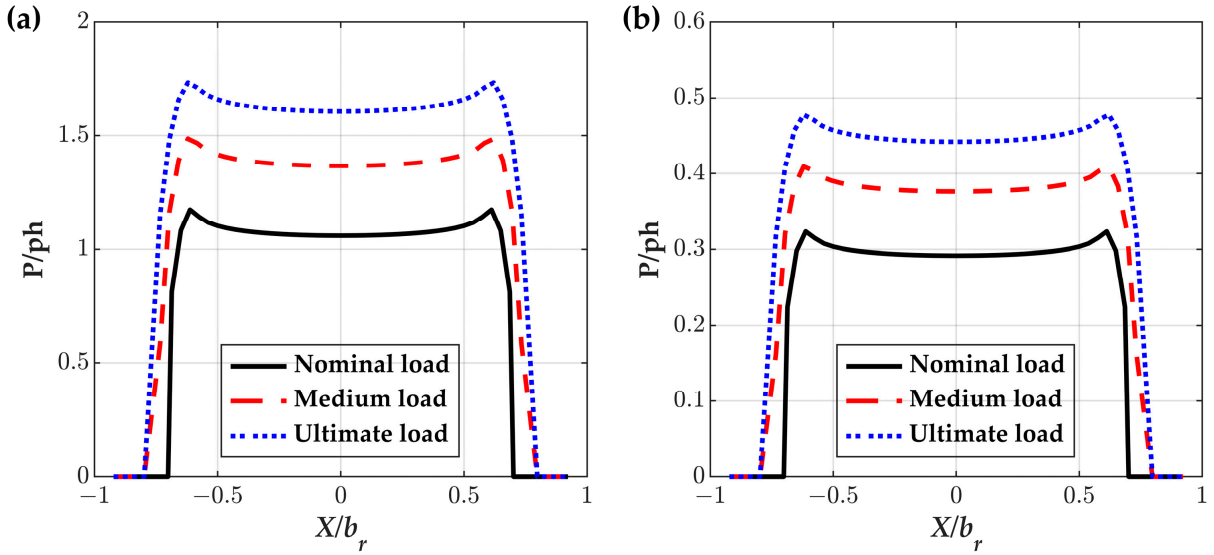

Figure 15. Pressure and shear stress distribution along the roller's axis considering varying operating load. (**a**) pressure distribution; (**b**) maximum shear stress distribution.

Figure 16 illustrates the optimal values of modification length *a* and modification quantity *b* which could induce the minimum oil film pressure considering various load values. With the increasing load, both the optimal modification length and optimal modification quantity rise. The result proves that a suitable roller's profile modification could reduce stress concentration induced by heavy loads.

Figure 17 depicts the oil film pressure and the maximum shear stress distribution along the roller's axis direction considering varying operating speeds. Nominal load is applied on the RV reducer and the load between roller and crankshaft is 1978 N. The sliding

velocities between the roller and crankshaft under nominal speed (1400 rpm), medium speed (2800 rpm), and ultimate speed (5600 rpm) are, respectively, 0.101 m/s, 0.221 m/s, 0.562 m/s. It can be concluded that the oil film pressure and the maximum shear stress are nearly the same under nominal speed and medium speed. The oil film pressure and the maximum shear stress increase slightly when the rolling speed increases to 5400 rpm. The results reveal that rolling speed has little impact on oil film pressure and maximum shear stress. In actuality, the reducer runs at the nominal rotational speed most of the time.

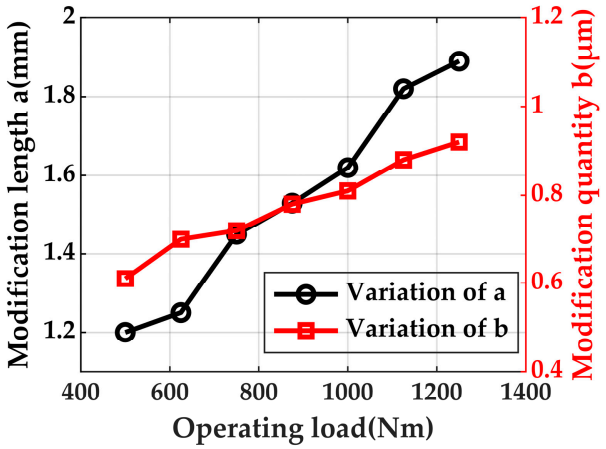

Figure 16. Optimal values of modification length *a* and modification quantity *b* considering various load values.

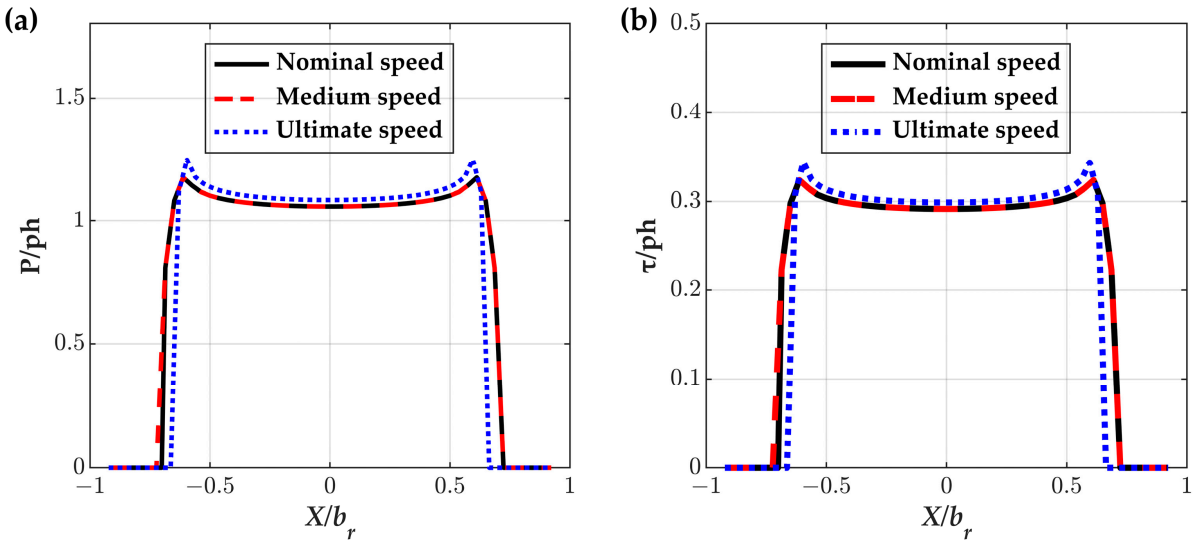

Figure 17. Pressure and shear stress distribution along the roller's axis considering varying operating speed. (**a**) pressure distribution; (**b**) maximum shear stress distribution.

Figure 18 depicts the optimal values of modification length and modification quantity considering various rolling speed values. It is obvious that the variation of optimal modification length and modification quantity can be neglected under different rolling speeds. This is because the sliding velocity is at a relatively low level and the oil film pressure is hardly affected by rolling speed.

One important thing to note is that the minimum oil film thickness under the cases above is more than 0.56 μm, which is much higher than the surface roughness (Ra 0.1 μm) of rollers and crankshaft. The result indicated that the rollers and crankshaft work in a full-film regime.

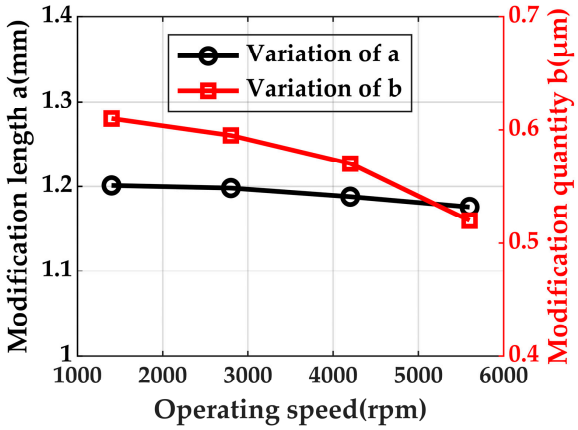

Figure 18. Optimal values of modification length and modification quantity considering various rolling speed values.

4. Experimental Results for Eccentric Bearings

Figure 19 depicts the damage on the crankshaft induced by three types of roller profile modification. The three types of roller profile modifications are arc generatrix (500 mm), straight generatrix and combined generatrix (a = 1.23 mm, b = 6 μm), respectively. A test rig for RV reducer was accomplished to conduct the durability test as shown in Figure 19a. A motor with maximum rotational speed of 6000 rpm and 7 kW power was used to drive the reducer. The load of the reducer was applied by a magnetic powder brake whose range is 0–2000 Nm. The experiments are conducted as follows: (1) The motor runs at a speed of 500 rpm without load for 1 h; (2) The load gradually rises from 0 Nm to an extreme value (1250 Nm) and the process takes 3 h; (3) The rotational speed gradually rises to 1400 rpm in 3 h; (4) Finally, the durability test is conducted under the extreme working condition for 300 h. The extreme load is adopted in order to accelerate the testing process. Castro ALR was used as the lubricating oil in the durability test. The durability experiments for the RV reducer with each type of roller profile were repeated three times.

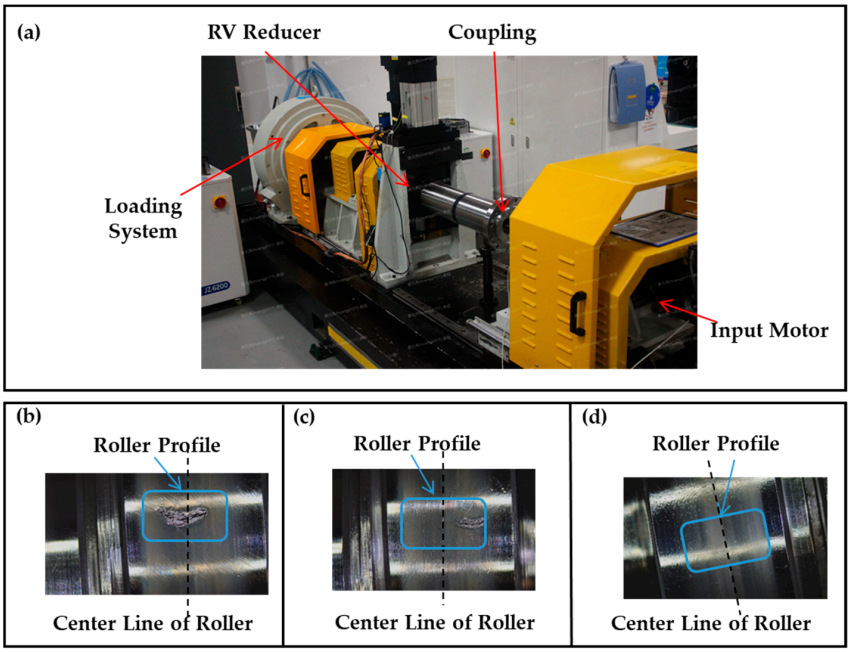

Figure 19. Fatigue damage induced by the three types of roller profile modification. (**a**) durability test rig for RV reducer; (**b**) arc generatrix shape roller; (**c**) straight generatrix shape roller; (**d**) combined generatrix shape roller.

In Figure 19b–d, the blue line represents the roller's profile. As one can see, spalling is located at the central region of the contact area between the roller and crankshaft in the case of arc generatrix shape roller (Figure 19b). As the roller's profile turns to a straight generatrix, spalling occurs near the edge of the contact area which proves that fatigue initiates from the site (Figure 19c). Yet in the case of a combined generatrix roller, it is clear that small pitting is distributed homogeneously all over the contact area (Figure 19d). The fatigue damage observed above is in good accord with the oil film pressure calculated by the numerical method adopted in Section 2 (Figure 20). The theoretical and experimental results found solid support for the effect of combined generatrix on declining stress concentration and prolonging fatigue life.

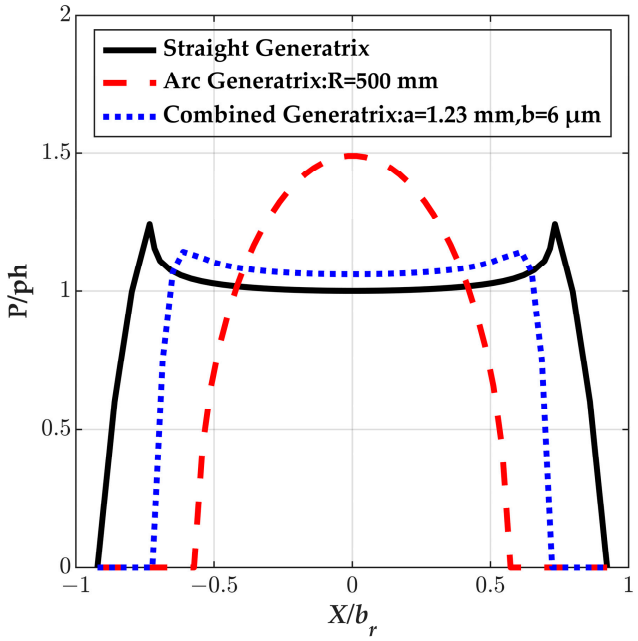

Figure 20. Numerical results of oil film pressure for three types of profile modification.

5. Conclusions

In this paper, a novel numerical methodology is established through the integration of a finite element model (FEM) with elastohydrodynamic lubrication (EHL) analysis. This approach facilitates a comprehensive examination of the ramifications of modifying the profile of rollers, as well as the impact of various operational conditions on system performance. The key findings derived from this research are summarized below:

(1) The influence of cycloidal gear flexibility on the load distribution across bearings is significant, with the finite element model indicating a 15% increase in maximum load compared to the rigid model;

(2) Stress concentration is found at the two ends of the roller with straight generatrix and the edge effect is severe. In the case of an arc generatrix shape roller, maximum pressure and shear stress are generated at the center of the roller and the stress concentration is higher than that of the straight generatrix shape roller as the contact state is converted to point contact. The edge effect and stress concentration are weakened by adopting the combined generatrix on rollers. The most beneficial values of modification length and quantity can be obtained by the numerical method in this paper considering mechanical machining capability;

(3) With the increasing load, the oil film pressure and maximum shear stress of the bearing's rollers rise. There is a slight increase in oil film pressure and maximum shear stress with the increase in rotational speed as the RV reducer normally works at a relatively

low speed level. The optimal values of modification length and modification quantity under various load and rolling speed conditions were investigated;

(4) Durability testing on RV reducers, incorporating various roller profile modifications, demonstrates that a combined generatrix approach significantly reduces the stress concentration and extends the reducer's fatigue life, as evidenced by crankshaft damage morphology analysis.

Author Contributions: Conceptualization, X.Z.; methodology, X.Z. and W.C.; formal analysis, X.Z., G.W. and J.G.; investigation, G.W., D.W. and J.G.; software, D.W.; writing—original draft preparation, X.Z.; writing—review and editing, J.G.; supervision, W.C.; funding acquisition, W.C. All authors have read and agreed to the published version of the manuscript.

Funding: This work was funded by National Key R&D Program of China (2023YFB4705100).

Data Availability Statement: The original contributions presented in this study are included in the article. Further inquiries can be directed to the corresponding author.

Acknowledgments: The authors are deeply grateful to the Jiya Precision Machinery Technology Co., Ltd. for providing the experimental support.

Conflicts of Interest: Authors Xinyue Zhang, Gang Wang, Daqi Wu, Jian Guan and Wenjie Chen were employed by the company Midea Group. Authors declare that the research was conducted in the absence of any commercial or financial relationships that could be construed as a potential conflict of interest.

Nomenclature

E	modification length of the roller	q	contact friction
a_0	distributed radius of the crankshaft	r	radius of roller's round corner
a'	pressure–viscosity exponent	R	radius of roller's arc
b	modification quantity of the roller	r'_c	pitch circle radius of cycloidal gear pins
b_r	half value of the roller length	U	relative entraining speed of cycloidal gear and pins
b_w	contact half-width	V_e	elastic deformation
E'	equivalent elastic modulus	w	contact load of the contact area
f	clearance considering bodies' geometry before elastic deformation	Z'	pressure–viscosity index
$\boldsymbol{F}$	force vector of cycloidal gear pins	ρ	density of lubricant
$\boldsymbol{F_A}, \boldsymbol{F_B}, \boldsymbol{F_C}$	force vector of three eccentric bearings of cycloidal gear	ρ_0	lubricant density at ambient pressure
$\boldsymbol{F_t}$	tangential force of cycloidal gear and pins	η	effective viscosity of the lubricant
h_0	the normal gap of the two bodies	η_0	lubricant viscosity at ambient pressure
H	film thickness	Ω	the solution domain
K_L	stiffness of the roller	α_c	angle between $\boldsymbol{F}$ and $\boldsymbol{F_t}$
L_r	length of the roller	θ	rotational angle of crankshaft
P	oil film pressure	τ_{xz}	shear stress of sub-surface
ph	maximum contact pressure calculated by Hertzian contact theory	μ	friction coefficient
τ	maximum shear stress	T	torque on a single cycloidal gear
Re	Reynolds number	L	specific length of the contact region
P/ph	the dimensionless quantity of pressure	τ/ph	the dimensionless quantity of maximum shear stress
Q	contact load of roller and crankshaft	ε, ϑ	the integrating coordinates of solution domain Ω

References

1. Guan, J.; Wu, D.; Zhang, L.; Wang, G.; Chen, W.; Lin, W.; Zhao, H.; Bai, P.; Tian, Y.; Song, W. The friction behavior and wear mechanism of RV reducer gear steel (20CrMo) subjected to three different heat treatment processes from −20 °C to 100 °C. *J. Mater. Res. Technol.* **2024**, *32*, 2609–2623. [CrossRef]
2. Wang, H.; Shi, Z.; Yu, B.; Xu, H. Transmission performance analysis of RV reducers influenced by profile modification and load. *Appl. Sci.* **2019**, *9*, 4099. [CrossRef]
3. Zhang, T.; Li, X.; Wang, Y.; Sun, L. A semi-analytical load distribution model for cycloid drives with tooth profile and longitudinal modifications. *Appl. Sci.* **2020**, *10*, 4859. [CrossRef]
4. Ahn, H.J.; Choi, B.M.; Lee, Y.H.; Pham, A.D. Impact Analysis of Tolerance and Contact Friction on a RV Reducer using FE Method. *Int. J. Precis. Eng. Manuf.* **2021**, *22*, 1285–1292. [CrossRef]
5. Yang, W.; Tang, X.; Liang, Q. Tooth Surface Contact Analysis of Involute Rotate Vector Reducer Based on a Finite Element Linear Programming Method. *IEEE Access* **2019**, *7*, 176719–176731. [CrossRef]
6. Yang, M.; Zhang, D.; Cheng, C.; Han, X. Reliability-based design optimization for RV reducer with experimental constraint. *Struct. Multidiscip. Optim.* **2021**, *63*, 2047–2064. [CrossRef]
7. Qian, H.; Li, Y.; Huang, H. Time-variant reliability analysis for industrial robot RV reducer under multiple failure modes using Kriging model. *Reliab. Eng. Syst. Saf.* **2020**, *199*, 106936. [CrossRef]
8. Dion, J.L.; Pawelski, Z.; Chianca, V.; Zbigniew, Z.; Nicolas, P.; Grzegorz, U.; Janusz, O.; Grzegorz, M.; Xavier, L. Theoretical and experimental study for an improved cycloid drive model. *ASME J. Appl. Mech.* **2020**, *87*, 011002. [CrossRef]
9. Sensinger, J. Efficiency of high-sensitivity gear trains, such as cycloid drives. *ASME. J. Mech. Des.* **2013**, *135*, 071006. [CrossRef]
10. Jiang, N.; Wang, S.; Xie, X.; Yuan, X.; Yang, A.; Zhang, J. A vectorial modification methodology based on an efficient and accurate cycloid tooth profile model. *Precis. Eng.* **2022**, *73*, 435–456. [CrossRef]
11. Han, J.; Li, W.; Qiao, Z. Lubrication characteristics of cycloid pin wheel transmission of RV reducer. *J. Cent. South Univ.* **2021**, *28*, 398–417. [CrossRef]
12. Li, T.; An, X.; Deng, X.; Li, J.; Li, Y.L. A new tooth profile modification method of cycloidal gears in precision reducers for robots. *Appl. Sci.* **2020**, *10*, 1226. [CrossRef]
13. Xie, Y.; Xu, L.; Deng, Y. A dynamic approach for evaluating the moment rigidity and rotation precision of a bearing-planetary frame rotor system used in RV reducer. *Mech. Mach. Theory* **2022**, *173*, 104851. [CrossRef]
14. Meng, Y.; Wu, C.; Ling, L. Mathematical modeling of the transmission performance of 2K–H pin cycloid planetary mechanism. *Mech. Mach. Theory* **2007**, *42*, 776–790. [CrossRef]
15. Zhang, D.; Li, X.; Yang, M.; Wang, F.; Han, X. Non-random vibration analysis of rotate vector reducer. *J. Sound Vib.* **2023**, *542*, 117380. [CrossRef]
16. Yang, Y.; Zhou, G.; Chang, L.; Chen, G. A modelling approach for kinematic equivalent mechanism and rotational transmission error of RV reducer. *Mech. Mach. Theory* **2021**, *163*, 104384. [CrossRef]
17. Hidaka, T.; Wang, H.Y.; Ishida, T. Rotational transmission error of K-H-V planetary gears with cycloid gear (1st Report, Analytical method of the rotational transmission error). *JSME Int. J. C Mech. Syst.* **1994**, *60*, 645–653. [CrossRef]
18. Ishida, T.; Wang, H.Y.; Hidaka, T. Rotational transmission error of K-H-V planetary gears with cycloid gear (2nd report, effects of manufacturing and assembly errors on rotational transmission error,). *JSME Int. J. C Mech. Syst.* **1994**, *60*, 278–285. [CrossRef]
19. Wang, H.Y.; Ishida, T.; Hidaka, T. Rotational transmission error of K-H-V planetary gears with cycloid gear (3rd report, mutual effects of errors of the elements on the rotational transmission error,). *JSME Int. J. C Mech. Syst.* **1994**, *60*, 286–293. [CrossRef]
20. Guo, L.; Zhang, Z.; Wang, W.; Zhao, Y.; Wong, P. An explicit solution to a three-dimensional wedge problem considering two edges effect. *Friction* **2020**, *8*, 370–383. [CrossRef]
21. Zhang, C.; Gu, L.; Mao, Y.; Wang, L. Modeling the frictional torque of a dry-lubricated tapered roller bearing considering the roller skewing. *Friction* **2019**, *7*, 551–563. [CrossRef]
22. Gao, S.; Hou, X.; Ma, C.; Yang, Y.; Li, Z.; Yin, R.; Zhu, R. Transient simulation analysis of needle roller bearing in oil jet lubrication and planetary gearbox lubrication conditions based on computational fluid dynamics. *Lubricants* **2024**, *12*, 39. [CrossRef]
23. Marian, M.; Almqvist, A.; Rosenkranz, A.; Fillon, M. Numerical micro-texture optimization for lubricated contacts-A critical discussion. *Friction* **2022**, *10*, 1772–1809. [CrossRef]
24. Chen, H.; Wang, W.; Liang, H.; Zhang, H. Elastohydrodynamic lubrication analysis of tapered roller bearing considering effect of free ends. *Tribol. Int.* **2023**, *180*, 108304. [CrossRef]
25. Zhao, X.; Zhang, Y.; Cao, S. Evaluation and analysis of abrasive wear resistance of hybrid roller bearings under lubricant contamination. *Wear* **2024**, *558–559*, 205570. [CrossRef]
26. Liu, J.; Ding, S.; Pang, R.; Li, X. Influence of the roller profile modification of planet bearing on the vibrations of a planetary gear system. *Measurement* **2021**, *180*, 109612. [CrossRef]
27. Zhu, D.; Wang, J.; Ren, N.; Wan, J. Mixed elastohydrodynamic lubrication in finite roller contacts involving realistic geometry and surface roughness. *J. Tribol.* **2012**, *134*, 011504. [CrossRef]

28. Qiu, L.; Liu, S.; Chen, X.; Wang, Z. Lubrication and loading characteristics of cylindrical roller bearings with misalignment and roller modifications. *Tribol. Int.* **2022**, *165*, 107291. [CrossRef]
29. Xiang, G.; Yang, T.; Guo, J.; Wang, J.; Liu, B.; Chen, S. Optimization transient wear and contact performances of water-lubricated bearings under fluid-solid-thermal coupling condition using profile modification. *Wear* **2022**, *502–503*, 204379. [CrossRef]
30. Wang, R.; Behandish, M. Surrogate modeling for physical systems with preserved properties and adjustable tradeoffs. *arXiv* **2022**, arXiv:2202.01139. [CrossRef]
31. Wang, R.; Shapiro, V. Topological semantics for lumped parameter systems modeling. *Adv. Eng. Inform.* **2019**, *42*, 100958. [CrossRef]
32. Wen, C.; Bai, P.; Zhang, H.; Zhang, S.; Meng, X.; Meng, Y.; Tian, Y. Theoretical model development and mixed lubrication analyses of rolling piston type rotary compressors: A Review. *Lubricants* **2024**, *12*, 273. [CrossRef]
33. Li, W.; Tian, J. Unsteady-state temperature field and sensitivity analysis of gear transmission. *Tribol. Int.* **2017**, *116*, 229–243. [CrossRef]
34. Wang, L.; Cui, L.; Zheng, D.; Gu, L. Nonlinear dynamics behaviors of a rotor roller bearing system with radial clearances and waviness considered. *Chin. J. Aeronaut.* **2008**, *21*, 86–96. [CrossRef]
35. Liu, X.; Yang, P. Analysis for finite line contacts of thermal elastohydrodynamic lubrication. *Tribology* **2002**, *22*, 295–299. [CrossRef]
36. Wen, B. *Machine Design Handbook*, 5th ed.; China Machine Press: Beijing, China, 2010; pp. 9, 83–111.
37. Johnson, K.L. *Contact Mechanics*, 1st ed.; Cambridge University Press: Cambridge, UK, 1985; pp. 12–23.